

Article

Microstructure and Properties of a Novel Al-Mg-Si Alloy AA 6086

Franc Zupanič^{1,*} , Matej Steinacher², Sandi Žist² and Tonica Bončina¹¹ Faculty of Mechanical Engineering, University of Maribor, SI-2000 Maribor, Slovenia; tonica.boncina@um.si² Impol d.d., SI-2310 Slovenska Bistrica, Slovenia; matej.steinacher@impol.si (M.S.); sandi.zist@impol.si (S.Ž.)

* Correspondence: franc.zupanic@um.si; Tel.: +386-2-220-7863

Abstract: In this work, we investigated a novel Al-Mg-Si alloy, which was developed from an AA 6082, in order to considerably improve the yield and tensile strengths whilst retain excellent ductility. The new alloy possesses a higher content of Si than specified by AA 6082, and, in addition, it contains copper and zirconium. The alloy was characterized in the as-cast condition, after homogenization, extrusion, and T6 heat treatment using light microscopy, scanning and transmission electron microscopy with energy dispersive spectrometry, X-ray diffraction, differential thermal analysis and tensile testing. After T6 temper, tensile strengths were around 490 MPa with more than 10% elongation at fracture. The microstructure consisted of small-grained Al-rich matrix with α -AlMnSi and Al₃Zr dispersoids, and Q'-AlCuMgSi and β -Mg₂Si-type precipitates.

Keywords: aluminium; ageing; microstructure; tensile strength

Citation: Zupanič, F.; Steinacher, M.; Žist, S.; Bončina, T. Microstructure and Properties of a Novel Al-Mg-Si Alloy AA 6086. *Metals* **2021**, *11*, 368. <https://doi.org/10.3390/met11020368>

Academic Editor: Marcello Cabibbo

Received: 30 January 2021

Accepted: 19 February 2021

Published: 23 February 2021

Publisher's Note: MDPI stays neutral with regard to jurisdictional claims in published maps and institutional affiliations.



Copyright: © 2021 by the authors. Licensee MDPI, Basel, Switzerland. This article is an open access article distributed under the terms and conditions of the Creative Commons Attribution (CC BY) license (<https://creativecommons.org/licenses/by/4.0/>).

1. Introduction

The manufacturing of green vehicles, characterized by lower fuel consumptions and CO₂ emissions, is a must for the automotive industry. This can be achieved through a reduction of the vehicle weight by replacing heavier steel parts with lighter, high-strength and, at the same time, ductile aluminium alloys. Al-Mg-Si alloys (series 6xxx), in particular, can be used [1]. Some of them are used for parts that require excellent crash performance [2]. There are also attempts to improve the mechanical properties of Al-Si-Mg alloys [3–5]. Table 1 gives tensile properties of some Al-alloys, which shows that the required properties of AA 6610A are highest among Al-Mg-Si alloys.

Table 1. The required mechanical properties of 6xxx alloys in T6 temper according to EN 755-2 standard.

Alloy	R _{p0.2} /MPa	R _m /MPa	A/%
AA 6082	min. 260	min. 310	min. 8
AA 6182	min. 330	min. 360	min. 9
AA 6110A	min. 380	min. 410	min. 10

Al-Mg-Si alloys are typical precipitation hardening alloys. The strengthening effect in Al-Mg-Si alloys is achieved through β' and β'' precipitates [6–8]. These precipitates are metastable variants of the equilibrium Mg₂Si phase. They turn to Mg₂Si when the alloy is held prolonged at higher temperatures (between the ageing and solvus temperatures). One obtains a combination of 6xxx and 2xxx alloy by the addition of copper to Al-Mn-Si. In these alloys, the phase Q-AlCuMgSi dominates but not Θ -Al₂Cu that is predominant in 2xxx alloys. During ageing, Q' precipitates are formed in the α -Al, which strengthen the matrix in addition to β'' precipitates [9–11].

Zirconium can decrease the size of crystal grains during solidification. However, zirconium in the alloy can reduce the efficiency of Al-Ti-B grain refiners due to the poisoning

of TiB_2 and Al_3Ti heterogeneous nucleation sites [12]. It is essential that zirconium form Al_3Zr dispersoids at higher temperatures [13–16]. These dispersoids considerably decrease the tendency to crystal growth during heat treatment and hot plastic deformation. In this way, zirconium contributes to strengthening of the alloys by dispersion hardening and hardening by grain boundaries. Namely, the latter hardening is essential when the crystal grains are fine [17,18].

This study's main aim was to produce a new high-strength Al-Mg-Si alloy under industrial conditions (semi-continuous casting, homogenization, extrusion and T6 temper), to determine its microstructure after each step of the manufacturing process and its tensile properties.

2. Materials and Methods

The alloy AA 6086 [19] was developed from the AA 6082. The main differences are in the contents of Si, Cu and Zr. The AA 6082 contains 0.7–1.3 wt.% Si, while the AA 6086 contains 1.3–1.7 wt.% Si. The higher silicon content can contribute to a higher fraction of Mg_2Si -based precipitates in the microstructure. The increase in Cu-content from 0.1 to 0.8 wt.% Cu (0–0.1 wt.% Cu in AA 6082) can provoke Cu-rich precipitates' formation, which can further increase the precipitation hardening effect. The addition of Zr in the range from 0.15–0.25 wt.% Zr can promote the formation of Al_3Zr dispersoids, which can reduce grain growth during homogenization and solution treatment and increase grain strengthening. One of the possible primary applications of this alloy is to produce automobile steering tie rods, which require high-strength and ductility.

The 20 t charge of the alloy was prepared in an induction furnace (Otto Junker GmbH, Simmerath-Lammersdorf, Germany) at a temperature of 760 °C. The zirconium was added with the master alloy AlZr10. The melt was poured into a holding furnace (Otto Junker GmbH, Simmerath-Lammersdorf, Germany) for 90 min at temperatures between 730 and 740 °C. The billets with a diameter of 282 mm were semi-continuously cast using the AirSlip Casting Technology (Wagstaff Inc, Spokane Valley, WA 99216 USA). AlTi5B1 grain refiner was added during casting. The chemical composition of the alloy is given in Table 2. The billets were homogenized at 530 °C for 5 h and then extruded on 55 MN direct extrusion press (GIA Clecim Press, Albacete, Spain) into bars with a diameter of 57 mm. The extrusion rate was 7 m/min and extrusion ratio 4.95. After extrusion, the bars were solution treated at 530 °C for 2 h and then artificially aged at 180 °C for 8 h (T6 temper).

Table 2. The chemical composition of the alloy AA 6086 in wt.%, as determined by ICP-OES (Thermo ARL 4460 Optical Emission Spectrometer, ThermoFisher Scientific, Waltham, MA, USA).

Alloy	Al	Si	Fe	Cu	Mn	Mg	Cr	Zn	Ti	Zr
AA 6082	Remain	0.92	0.26	0.07	0.56	0.70	0.14	0.03	0.02	0.01
AA 6086	Remain	1.58	0.18	0.55	0.71	1.01	0.19	0.17	0.04	0.17

The differential thermal analysis (DTA) was carried out using Mettler Toledo 851 (Mettler Toledo, Columbus, Ohio 43240, USA). A sample was heated and cooled at a rate of 10 °C/min. The samples in the as-cast condition were examined metallographically using a light microscope Nikon EPIPHOT 300 (Tokyo, Japan), and a scanning electron microscope (SEM) Sirion 400 NC (FEI, Eindhoven, Netherlands). In SEM, we also carried out microchemical analysis using energy dispersive spectroscopy—EDS (Oxford Analytical, Bicester, UK). Samples for grain analysis were prepared on Struers Lectropol (Struers, Ballerup, Denmark) using Barker's etchant (50 mL HBF_4 (48%) + 950 mL H_2O at 25 V for 90 s). The analysis was performed under the 50× magnification according to a standard ASTM E112-intercept method. X-ray diffraction was done at synchrotron Elettra (Trieste, Italy), using X-rays with a wavelength of 0.099996 nm. Thermo-Calc software (Thermo-Calc software AB, Solna, Sweden) and database TCAL5 were used to simulate solidification according to the Scheil model [20] and calculate equilibrium phases as a function of temperature.

Lamellae for transmission electron microscopy (TEM) were prepared using a focused ion beam (FIB by FEI, Helios) for the as-cast and heat-treated specimens. High-resolution TEM (HRTEM), and energy-dispersive X-ray spectroscopy (EDXS) were carried out in an FEI Titan 80–300 (FEI, Eindhoven, Netherlands) image corrected electron microscope.

Four tensile specimens of alloy AA 6086 and seventeen of alloy AA 6082 were tested. They were taken at $D/4$ in the longitudinal direction. The diameter of the specimens was 20 mm and the gauge length 100 mm. The tensile tests were done by Zwick Z250 (Zwick-Roell Testing Systems GmbH, Fürstenfeld, Austria) according to ISO 6892-1 standard.

3. Results

3.1. Phase Identification in the As-Cast Condition and after Homogenization

Figure 1 gives the calculated phase composition and the effect of Zr on the liquidus temperature. The modelled liquidus temperature is around 700 °C when the alloy contains 0.15% Zr and rises to about 740 °C at 0.25% Zr. Thus, the alloy can be melted entirely in typical industrial furnaces, which can attain temperatures slightly above 750 °C. On the other hand, the effect on the solidus temperature is rather low, which remains faintly higher than 550 °C at Zr-contents up to 0.4%.

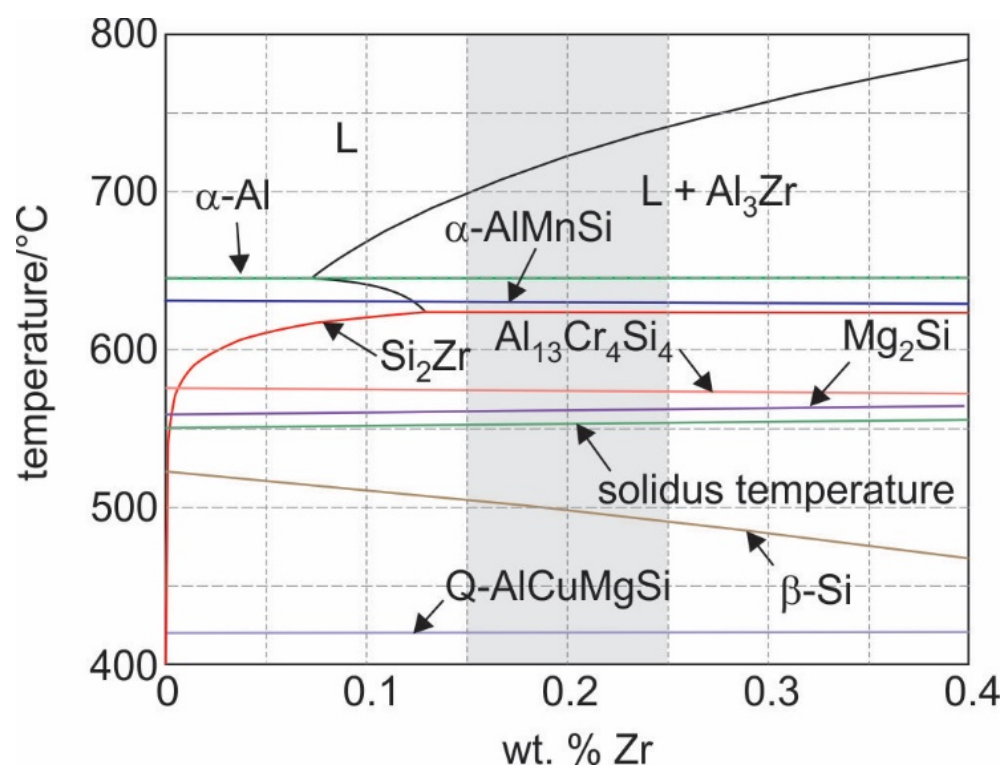


Figure 1. The effect of Zr on the liquidus temperature and formation of phases in the Al-corner. The shaded area indicates the content range of Zr in AA 6086, the contents of other elements are the same as in Table 2.

DTA-analysis (Figure 2) showed that the incipient melting point was at approximately 540 °C, which is more than 10 °C lower than the calculated solidus temperature. This is the result of non-equilibrium solidification. Scheil simulation showed that during solidification also Θ -Al₂Cu, β -Si and Q-AlCuMgSi can form. Figure 1 shows that β -Si and Q-AlCuMgSi can form in the solid-state, and Θ -Al₂Cu is not predicted as a stable phase. DTA-analysis also suggests that the homogenization temperature should be below the incipient melting point below 540 °C.

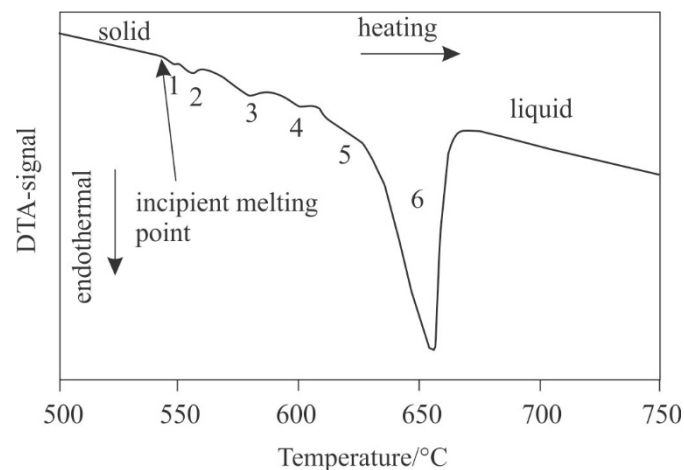


Figure 2. A section of the heating DTA-curve between 500 °C and 750 °C (the heating rate 10 °C/min, argon) showing six peaks occurring during the melting of the alloy, and that the incipient melting point lies approximately at 540 °C.

Figure 3 shows the light micrographs revealing the grain structure in the as-cast state and after homogenization treatment. The matrix α -Al solid solution possessed equiaxed dendritic grains with sizes between 180 and 215 μm . The grain structures were somewhat similar in both conditions.

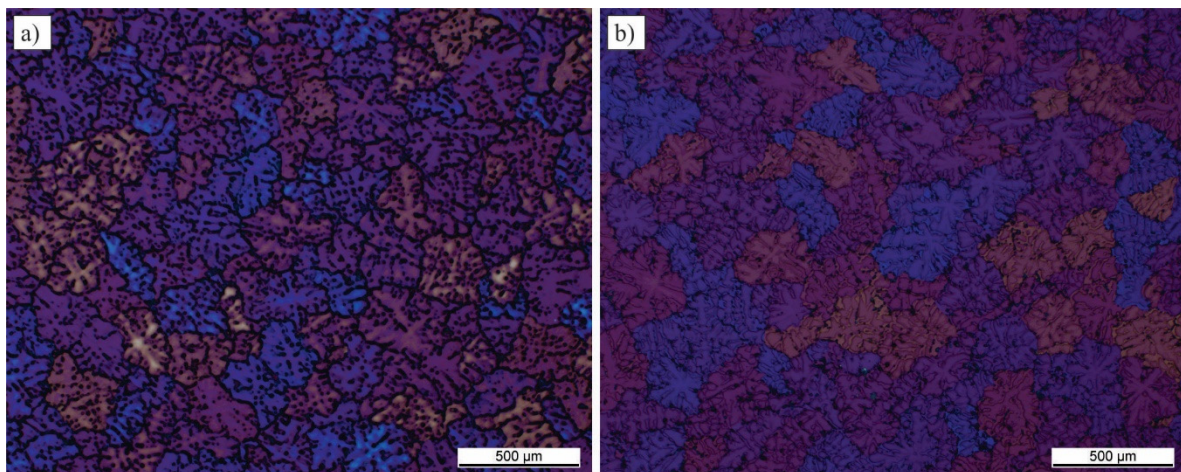


Figure 3. The light micrographs of the alloy AA 6086 in (a) the as-cast condition and (b) after homogenization treatment.

SEM-micrographs (Figure 4) revealed the presence of other phases in the interdendritic regions. The EDS-analysis showed that α -Al contained from 96.1 to 97.7 wt.% Al. At the centre of α -Al, the contents of Si and Cr were higher than in the interdendritic regions, the contents of Mg and Mn was less at the centre, while the contents of Cu and Zr were almost the same. The distribution of elements was uniform after homogenization. The contents of Si and Cr in the α -Al increased, the contents of Mg and Mn decreased, while almost no differences were observed in the Zr-content. X-ray diffraction revealed that the lattice parameters of the face-centred cubic FCC α -Al in both conditions were nearly the same ($a = 0.40458 \pm 0.00025$ nm in the as-cast state and $a = 0.40475 \pm 0.00020$ nm after homogenization, 0.004 nm smaller than in pure Al).

The X-ray diffraction patterns contained many peaks that often overlapped with one another. A detailed X-ray diffraction (XRD) analysis (Figure 5) revealed seven phases in the as-cast condition: α -Al, MgSi_2 , tetragonal Al_3Zr , α -AlMnSi, ZrSi_2 , Θ - Al_2Cu and β -Si and four after α -Al, MgSi_2 , tetragonal Al_3Zr , α -AlMnSi, ZrSi_2 , indicating that Θ - Al_2Cu and β -Si were dissolved. Nevertheless, the diffraction peaks remained at the same positions,

because α -AlMnSi have a very high number of diffractions peaks at lower angles due to its very large unit cell. The relative height of some peaks changed, indicating that some phases partly or entirely dissolved.

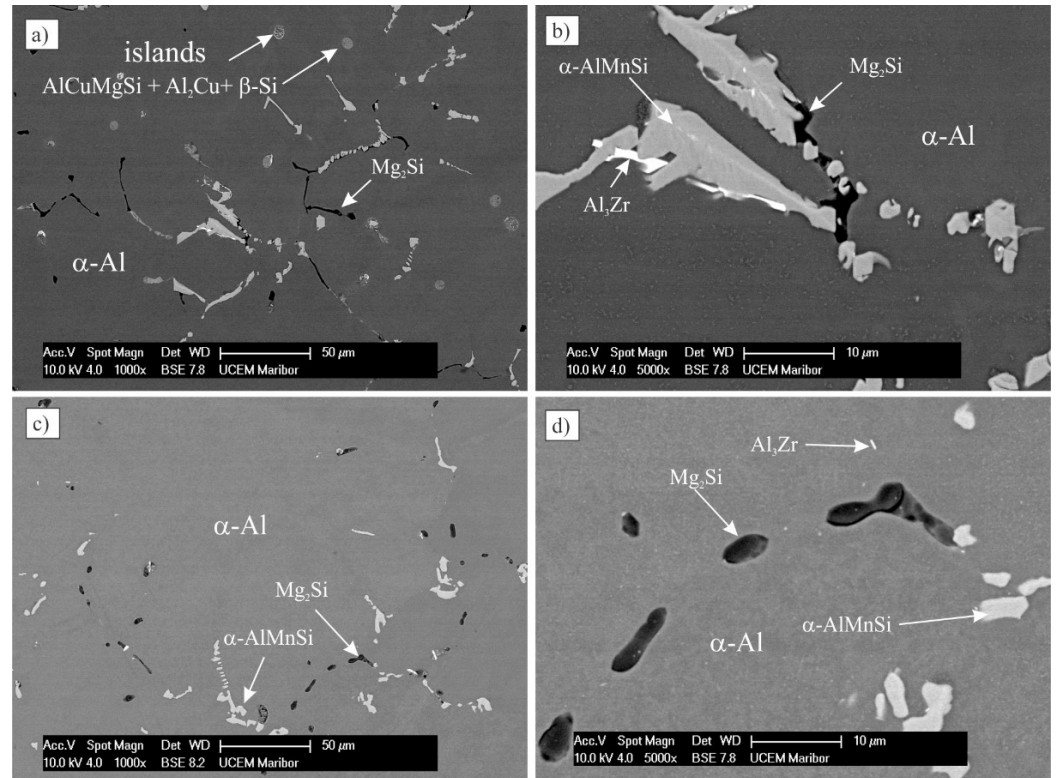


Figure 4. The backscattered electron micrographs (SEM) of the alloy AA 6086 in the as-cast condition (a,b) and after homogenization treatment (c,d).

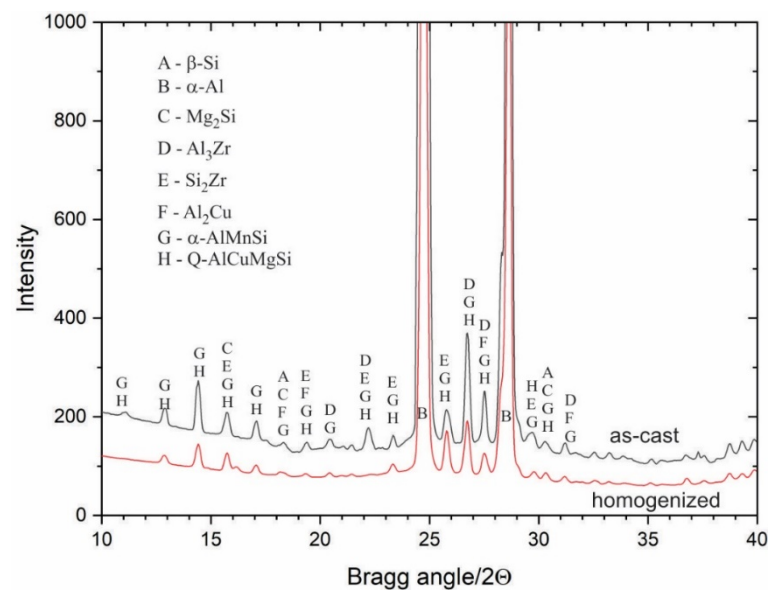


Figure 5. X-ray diffraction patterns of AA 6086 in the as-cast condition and after homogenization treatment. The peak positions of all phases found in the microstructure are indicated, showing strong overlapping of peaks.

Among the intermetallic phases, the volume fraction of the cubic α -AlMnSi was highest. EDS analysis confirmed that this phase also contained Fe and Cr. Typical chemical composition was 11–12 at.% Si; 2–5 at.% Cr, 11.8–12.6 at.% Mn, 8–10 at.% Fe, 0.5 at.% Cu and traces of Zr. The phase α -AlMnSi was present in the interdendritic and intergranular spaces. It has the same composition in both conditions, so the lattice parameters were almost the same (α -Al(Mn,Fe)Si: as-cast $a = 1.26165 \pm 0.00410$ nm and homogenized $a = 1.26287 \pm 0.00397$ nm). The size of α -AlMnSi did not change significantly after homogenization. However, the particles became more compact, with rounded edges. The calculation of equilibrium phases (Figure 6) shows that α -AlMnSi is relatively stable in this alloy. Only a small fraction of α -AlMnSi dissolves when heated to the homogenization temperature. The particles coarsen slowly to decrease the interfacial energy. It also indicates that the alloying elements in α -AlMnSi cannot be dissolved in α -Al and contribute to dispersion and precipitation hardening.

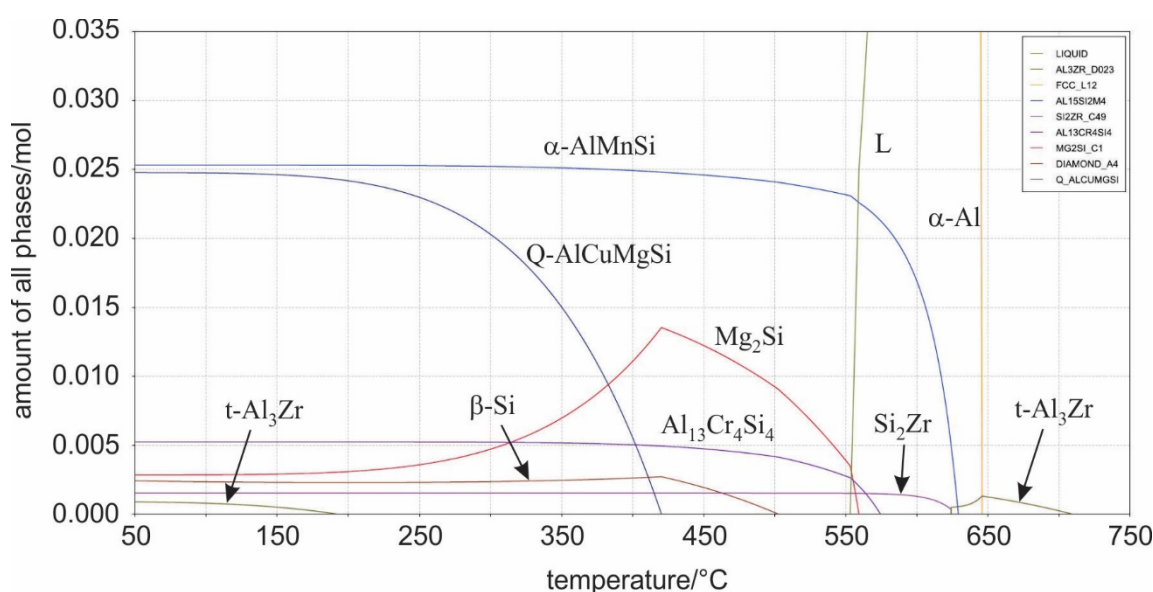


Figure 6. The calculated equilibrium phase fractions as a function of temperature. The calculated equilibrium solidus temperature T_s was slightly above 750 °C. The $\text{Al}_{13}\text{Cr}_4\text{Si}_4$ phase was not observed in the microstructure, as chromium did not form its own phase, but it was incorporated into α -AlMnSi.

The black Mg_2Si had a shape of Chinese script within a two-phase (α -Al + Mg_2Si) structure in the as-cast condition. During non-equilibrium solidification, an excess of Mg_2Si forms due to Mg and Si segregation in the interdendritic region. The calculation showed (Figure 6) that Mg_2Si should dissolve in a more significant amount at homogenization temperature. The diffusivities of Mg and Si in α -Al are high [21], so the non-equilibrium amount of Mg_2Si can dissolve at the homogenization temperature and distribute in entire α -Al grains. It was shown that the volume fraction of Mg_2Si dropped from 1.4% to 0.3% after homogenization, and the remaining particles significantly change their shape. They also became spheroidal in shape to decrease the interfacial energy. The dissolved Mg and Si are critical for the precipitation of β -type precipitates during artificial ageing. The lattice parameters were similar in both conditions (as-cast $a = 0.63483 \pm 0.00360$ nm and homogenized $a = 0.63422 \pm 0.00126$ nm).

Zirconium was present in platelike particles of the tetragonal Al_3Zr and within the orthorhombic Si_2Zr . Si_2Zr crystallized on the Al_3Zr platelets and was not separated from Al_3Zr . The closer microstructure analysis revealed that $\beta\text{-Si}$, Al_2Cu and Q-AlCuMgSi were present within the islands formed via a multiphase reaction at the terminal stages of solidification (Figure 4a). The Scheil solidification model predicted all discovered phases [20]. Phases $\beta\text{-Si}$, Al_2Cu and Q-AlCuMgSi present within the islands in the as-cast condition, dissolved completely during homogenization, which is in accordance with calculations (Figures 1 and 6).

Within $\alpha\text{-Al}$, copious nucleation of dispersoids took place during homogenization (Figure 7). The TEM-investigation that $\alpha\text{-AlMnSi}$ and Al_3Zr dispersoids formed within the $\alpha\text{-Al}$ matrix during homogenization. Their sizes were between 100 and 500 nm, and had different shapes. They formed because of the supersaturation of the matrix with Zr and Mn after solidification. A detailed EDS-analysis showed that the most of dispersoids can be attributed to $\alpha\text{-AlMnSi}$ phase. The brighter phases in the BSE-SEM images, as well as in the HAADF TEM micrographs were identified as Al_3Zr dispersoids.

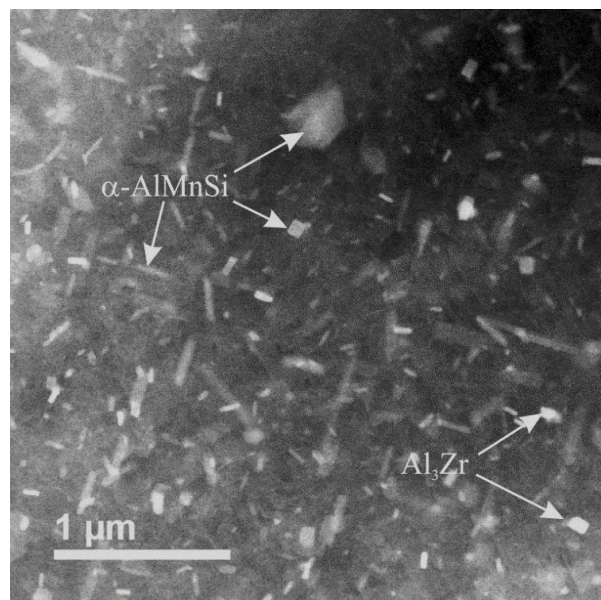


Figure 7. Dispersoids in $\alpha\text{-Al}$ after homogenization. The High-Angle Annular Dark Field (HAADF) image in TEM.

3.2. Microstructure of AA 6086 in the T6 Temper

The final microstructure and properties were achieved by the T6 temper, which consisted of the solution annealing and artificial ageing. Prior to this, the alloy was hot extruded, which oriented crystal grains in the pressing direction (length around $500\ \mu\text{m}$, thickness about $40\ \mu\text{m}$). Figure 8 shows a TEM-micrograph, which reveals the subgrain structure and dispersoids. During solution annealing, the crystal grains remain almost the same as after extrusion, but the subgrains became equiaxed (Figure 9). Since the subgrain sizes were only $2\text{--}5\ \mu\text{m}$ in size, dispersoids effectively prevented excessive grain growth during solution treatment. Extensive EDS-analysis also revealed two types of dispersoids, which were identified before: $\alpha\text{-AlMnSi}$ and Al_3Zr .

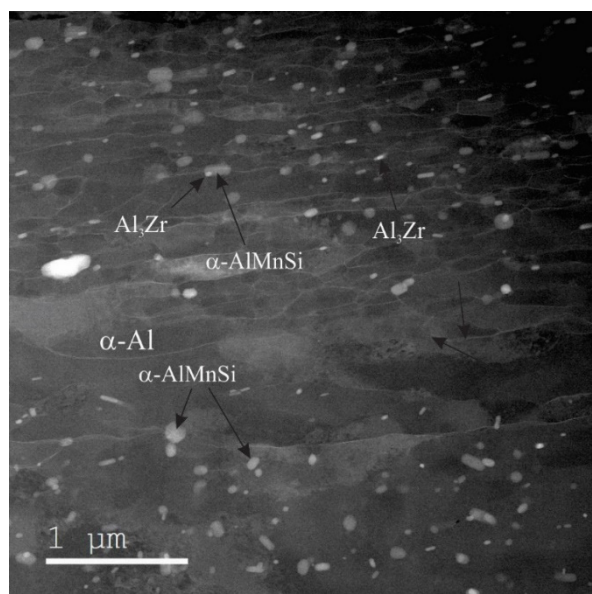


Figure 8. The microstructure after extrusion. The extrusion direction is from left to right. The High-Angle Annular Dark Field (HAADF) image in TEM.

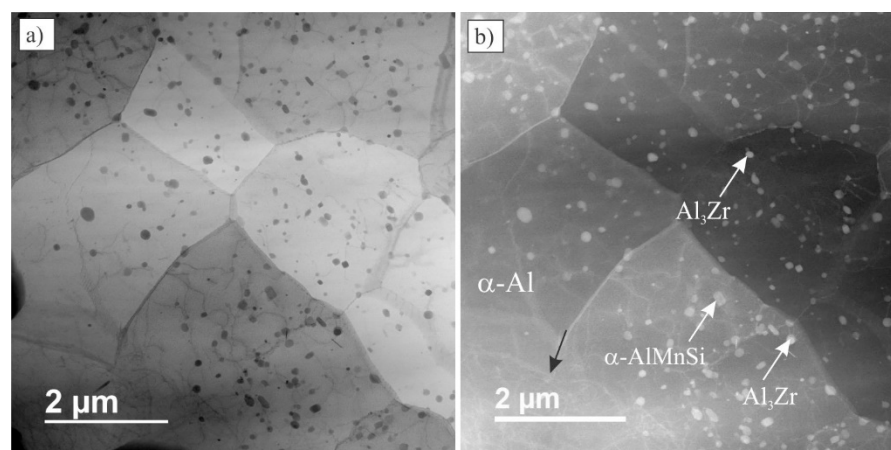


Figure 9. The transmission electron micrographs of the alloy after T6 temper, showing subgrains and the distribution of dispersoids. (a) Bright-field micrograph and (b) HAADF micrograph.

Figure 10 showed the analysis of an α -AlMnSi dispersoid. EDS showed that it also contained Cr and Fe. This particle had the z-axis parallel to the z-axis of Al, however, in the plane x - y no matching was found between these two phases.

Figure 11 showed the analysis of Al_3Zr dispersoid. EDS showed that it also contained silicon and a smaller amount of Ti, so it is correct to write $(\text{Al},\text{Si})_3\text{Zr}$ [17]. This particle possessed an excellent matching with the α -Al, which can be shown by HR-TEM micrograph (Figure 11c) and FFF of HR-TEM (Figure 11d). It is inferred that this particle had cubic L_{12} , which usually has the cube-to-cube orientation relationship with α -Al [22]. In addition to spheroidal Al_3Zr with L_{12} structure, platelike Al_3Zr particles were present. These particles had the same composition, but according to other works, they probably had a tetragonal structure [14].

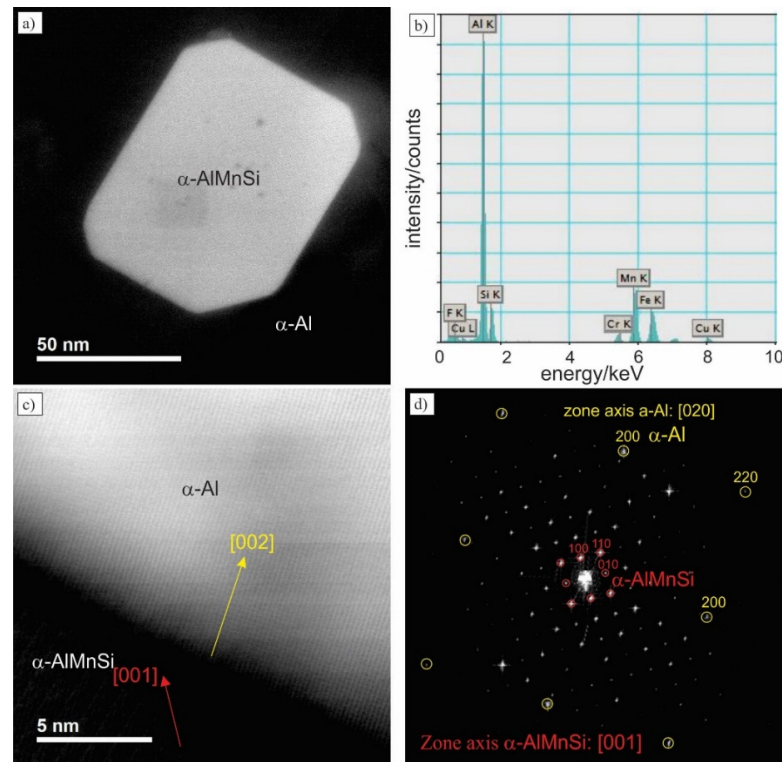


Figure 10. An α -ALMnSi dispersoid in the alloy after T6 temper. (a) HAADF micrograph, (b) EDS-spectrum, (c) High-resolution HAADF micrograph, (d) Fast-Fourier transform (FFT) of image (c). Zone axis α -Al: [001], zone axis of α -ALMnSi: [001].

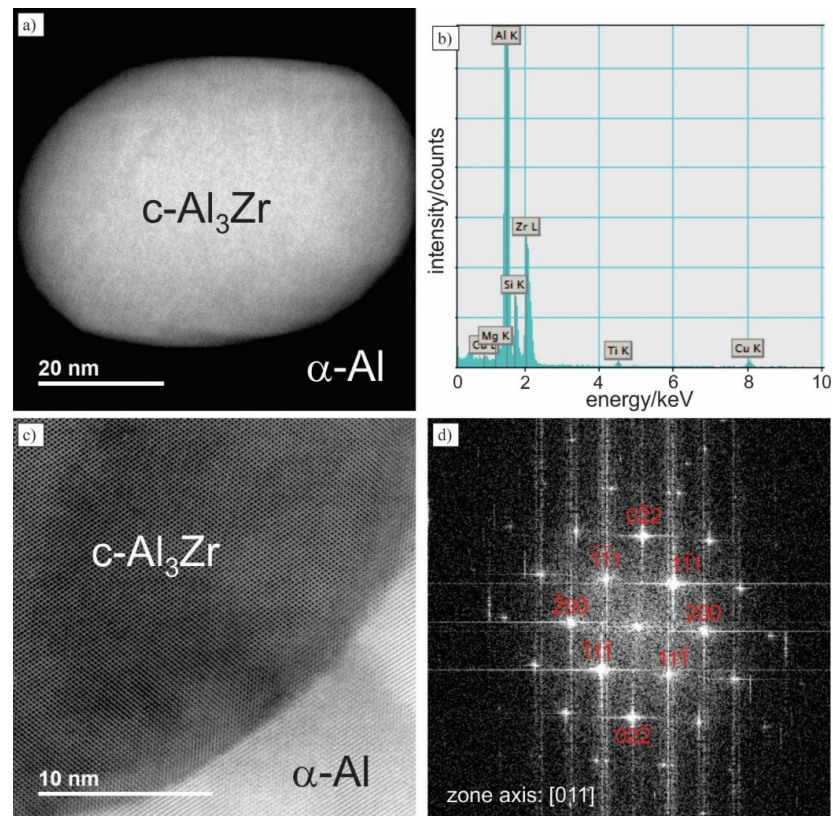


Figure 11. An c -Al₃Zr dispersoid in the alloy after T6 temper. (a) HAADF micrograph, (b) EDS-spectrum, (c) High-resolution HAADF micrograph, (d) FFT of image (c). Zone axis of c -Al₃Zr: [011].

Higher magnification showed a very high density of precipitates, which were mainly elongated β' -precipitates (Mg_2Si) and Q' -precipitates with different shapes (AlCuMgSi) (Figure 12). Figure 13 shows an individual Q' -precipitate in the α -Al, EDS-showed that it contained Al, Cu, Mg and Si.

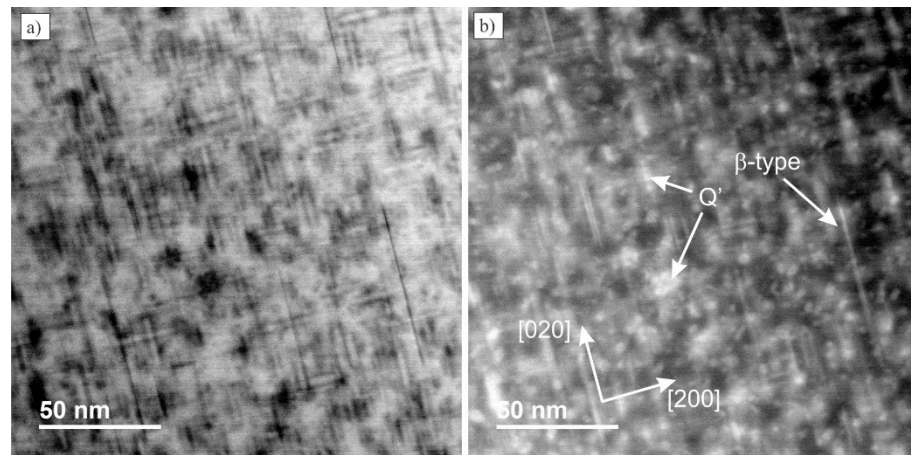


Figure 12. The transmission electron micrographs of the alloy after T6 temper, showing precipitates. (a) Bright-field micrograph and (b) HAADF micrograph.

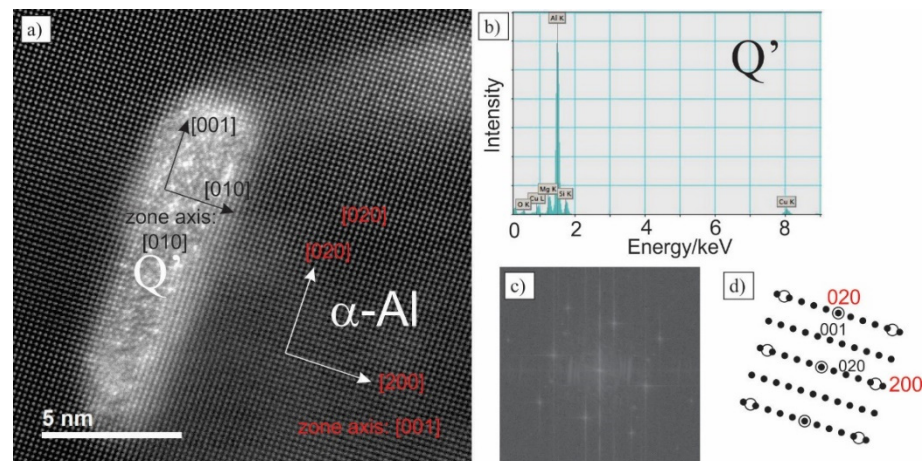


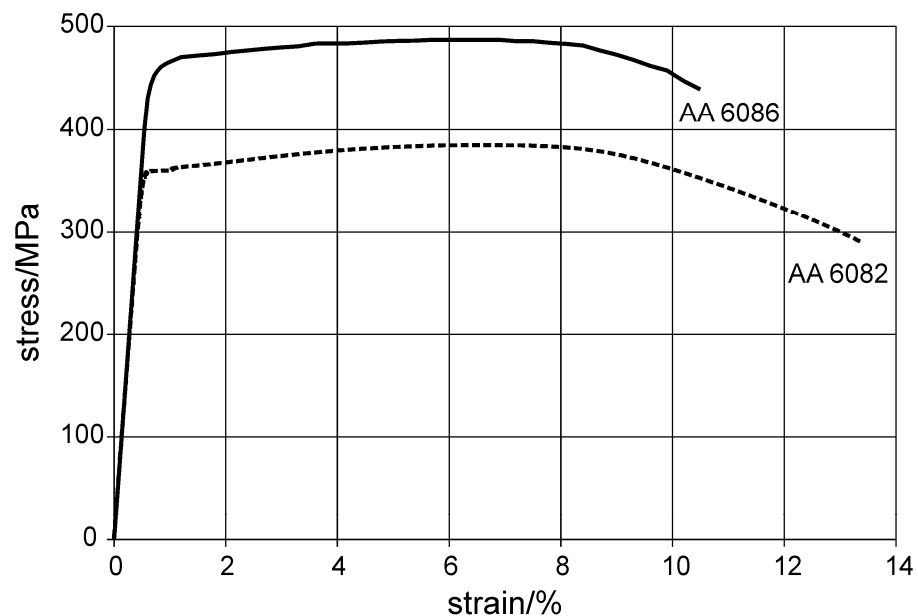
Figure 13. A Q' -precipitate. (a) The high resolution TEM micrograph of the Q' -precipitate in α -Al, (b) EDS-spectrum, (c) FFT of the HR-TEM micrograph, (d) model of FFT (Open circles: α -Al, black dots: Q' -precipitate).

3.3. Comparison of Tensile Properties of AA 6086 and AA 6082

The new alloy AA 6086 was developed by modifying the composition of AA 6082 to obtain higher strength. Table 3 compares the results of several tensile tests of both alloy and Figure 14 shows their typical stress-strain diagrams. The modification of chemical composition accompanied by typical manufacturing processes produced an increase of both 0.2 proof stress ($R_{p0.2}$) and tensile strength (R_m) for about 100 MPa, while the ductility did not change a lot.

Table 3. Comparison of tensile properties of AA 6082 (average values and standard deviations for 17 samples) and AA 6086 (average values and standard deviations for 4 samples).

Alloy	Sample	R _{p0.2} /MPa	R _m /MPa	A/%	
AA 6082	#1	365	389	13.7	
	#2	358	382	11.8	
	#3	354	376	13.2	
	#4	366	390	13.6	
	#5	359	384	14	
	#6	348	375	12.1	
	#7	362	386	13.5	
	#8	361	386	10.5	
	#9	358	384	13.1	
	graph	#10	360	385	13
		#11	359	384	14.2
		#12	358	385	12
		#13	359	385	11.5
		#14	363	387	9.8
		#15	377	401	12.8
		#16	371	395	11.3
		#17	373	396	13.3
Average and standard deviation		361.8 ± 6.8	386.5 ± 6.3	12.5 ± 1.2	
AA 6086	#1	450	490	12.3	
graph	#2	456	488	9.7	
	#3	461	492	12.4	
	#4	464	495	11.8	
Average and standard deviation		457.8 ± 5.3	491.2 ± 2.6	11.5 ± 1.1	

**Figure 14.** Typical tensile diagrams of the alloys AA 6082 (R_{p0.2} = 360 MPa, R_m = 385 MPa, A = 13.0%, blue) and AA 6086 (R_{p0.2} = 456 MPa, R_m = 488 MPa, A = 9.7%, red) in the T6 temper.

4. Discussion

By developing a novel alloy, the complete chemical composition of the AA 6082 was optimized [19]. The addition of Zr in the range 0.15–0.25% increased the liquidus temperature from about 650 °C to 700–740 °C, which requires sufficient superheating of the melt during melting, holding and casting to prevent formation of primary Al₃Zr. The particles can namely settle to the bottom of the furnace, and makes the Zr unavailable for formation of dispersoids in later manufacturing steps. It is also desirable that the cooling rates during

solidification are sufficiently high to avoid formation of coarse Al_3Zr crystals. Al_3Zr reacts with the liquid via a peritectic reaction, thus forming $\alpha\text{-Al}$ with a higher Zr-content. During further cooling $\alpha\text{-AlMnSi}$ forms via a eutectic reaction. The $\alpha\text{-AlMnSi}$ particles are rather coarse and prone to changes upon subsequent homogenization and solution treatment. Therefore, these particles can be detrimental for ductility. Mg_2Si is formed during further cooling. Despite it does not dissolve completely during homogenization, it obtains the spheroidal shape, which is not so harmful for the ductility. Other phases that form during the terminal stages of solidification completely dissolve during homogenization. Upon homogenization also dispersoids form. The alloying elements that are required for formation of dispersoids does not come from the dissolving phases formed during solidification, but rather from the $\alpha\text{-Al}$ matrix that was supersaturated with rather slowly diffusing Mn and Zr. Predominantly forms $\alpha\text{-AlMnSi}$ and Al_3Zr . In the first stage, $c\text{-Al}_3\text{Zr}$ forms [14], that was also identified in the investigated alloy. Cubic Al_3Zr can latter transform to tetragonal Al_3Zr . Plastic deformation with extrusion cause elongation of crystal grains in the extrusion direction. However, it also caused formation of elongated subgrains, which have only few micrometres in length and about $0.5\ \mu\text{m}$ in thickness. The solution treatment caused change of subgrains from directional to equiaxed, with sizes $2\text{--}5\ \mu\text{m}$. The dispersoids present in the matrix effectively prevented dynamic recovery and recrystallization during hot extrusion and excessive subgrain growth during solution annealing. Thus, the small subgrains can significantly contribute to hardening [17,18].

Artificial ageing caused the formation of β -type precipitates (Mg_2Si), which are the primary hardening precipitates in the Al-Mn-Si alloys. The addition of copper caused the formation of Cu-rich precipitates, e.g., $Q'\text{-AlCuMgSi}$, which were also found in other cases, when Cu was added to 6XXX alloys [11].

The combined effect of different hardening mechanisms produces a rather strong alloy. The yield strength was $452.5\text{--}463.1\ \text{MPa}$, the tensile strength $488.6\text{--}493.8\ \text{MPa}$, while elongation at fracture was $9.6\text{--}12.6\%$. The strength levels strongly exceed the strengths of other 6xxx alloys. However, the ductility was decreased, probably due to the coarse particles of $\alpha\text{-AlMnSi}$ phase. Therefore, additional work is required to further improve the properties, and determine impact toughness, fatigue strength and corrosion resistance of this alloy.

Table 4 gives the presence of precipitates and dispersoids in some Al-alloys. The basic and well-known alloy AA 6082 is strengthened mainly by β -type precipitates and contains $\alpha\text{-AlMnSi}$ dispersoids. The newer alloy AA 6182 has almost the same composition but contains $0.05\text{--}0.2\ \text{wt.}\%$ Zr. This increases the tensile strength by $50\ \text{MPa}$. It should be stressed that the alloy AA 6082 reached the tensile strength of $386\ \text{MPa}$ (Table 3), indicating that the alloy AA 6182 could attain strengths above $400\ \text{MPa}$. The alloy AA 6110A, which contains almost the same amount of copper as AA 6086, but no Zr, attains tensile strength $410\ \text{MPa}$. However, using the similar manufacturing route as in the current investigated AA 6086 alloy, tensile properties around $450\ \text{MPa}$ could be achieved. The novel alloy AA 6086 should contain more β -type precipitates, more Mn-dispersoids and, in addition, Zr-dispersoids. Altogether can contribute to higher strength levels in this alloy. The alloy AA 6086 is not yet included in EN 755-2:2016 standard, but its likely minimum tensile strength would be $450\ \text{MPa}$.

Table 4. The presence of precipitates and dispersoids in selected Al-alloys, and minimum tensile strengths R_m in T6 temper according to EN 755-2:2016 (* possible minimum value for AA 6086, which is not yet included in EN 755-2:2016; -: not present, +: present, ++: present in a higher amount).

Alloy	β -Type	Q' -Precipitate	Mn-Dispersoids	Zr-Dispersoids	min. R_m/MPa
AA 6082	+	-	+	-	310
AA 6182	+	-	+	+	360
AA 6110A	+	+	+	-	410
AA 6086	++	+	++	+	450 *

The investigated AA 6086 efficiently uses advantages of other high-strength Al-Mg-Si alloys, and is a result of evolution, and not revolution. It should be stated that for attaining the tensile strengths up to 500 MPa in Al-Mg-Si alloys no additional strengthening mechanisms are required. It should be stressed that in the industry, even classical manufacturing processes are tightly monitored and controlled, which allows obtaining the properties above the minimum levels stated by standards.

One of the examples of the drastic increase of mechanical properties with a slight change of composition was given by Han et al. [23] who studied microstructure and mechanical properties of Al-Mg-Si-Cu alloy with high manganese content. They achieved more than 50% increase in the yield strength of the examined alloys with high manganese content compared to the commercial AA 6061. They stated that additional Mn-dispersoids were generating the strong dispersion hardening effect.

5. Conclusions

The investigation results showed that a slight modification of the chemical composition of a standard aluminium alloy and its manufacturing by rather conventional manufacturing process steps could result in a much higher strength (about 100 MPa) with a minute decrease of ductility. Nevertheless, some improvements are still possible by optimization of processing steps.

The addition of copper resulted in the formation of Q'-AlCuMgSi precipitates, which combined with β -type (Mg_2Si) precipitates contributed to strong precipitation hardening effect. The addition of Zr resulted in the formation of different Al_3Zr -type dispersoids, which, together with α -AlMnSi prevented excessive grain growth during homogenization and solution treatment.

This work indicates that somewhat small changes can lead to significant variations in properties. This comprehension may lead to the development of other aluminium alloys with improved properties, which are highly required in today's world.

6. Patents

The results of this investigation were significant by the application of the following patent issued by European Patent Office: EP3214191A1: A high-strength Al-Mg-Si aluminium alloy and its manufacturing process, Peter Cvahte, Marina Jelen, Dragojevič Vukašin, Steinacher Matej, Impol d. d., Slovenska Bistrica, Slovenia

Author Contributions: Conceptualization, T.B., F.Z., M.S.; methodology, F.Z., M.S.; formal analysis, T.B., M.S., F.Z.; investigation, T.B., M.S. and S.Ž.; writing—original draft preparation, F.Z., T.B.; writing—review and editing, F.Z., T.B., S.Ž.; visualization, T.B. and M.S.; supervision, T.B. All authors have read and agreed to the published version of the manuscript.

Funding: The XRD investigations were carried out at Elettra, Sincrotrone Trieste, Italy, in the framework of Proposal 20180085. The TEM investigations at TU Graz were enabled by the ESTEEM 2 Project, which has received funding from the European Union's Seventh framework program under Grant Agreement No. 312483. The authors acknowledge the financial support from the Slovenian Research Agency (research core funding No. P2-0120 and I0-0029) and by the Ministry of Education, Science and Sport, Republic of Slovenia (Program MARTINA, OP20.00369).

Data Availability Statement: Not applicable.

Acknowledgments: We acknowledge Luisa Barba for support by XRD experiments at Elettra, Christian Gspan for S/TEM investigations.

Conflicts of Interest: The authors declare no conflict of interest.

References

1. McQueen, H.J.; Celliers, O.C. Application of hot workability studies to extrusion processing. 3. Physical and mechanical metallurgy of Al-Mg-Si and Al-Zn-Mg alloys. *Can. Met. Q.* **1997**, *36*, 73–86. [[CrossRef](#)]
2. Schiffl, A.; Schiffl, I.; Hartmann, M.; Brötz, S.; Österreicher, J.; Kühlein, W. Analysis of Impact Factors on Crash Performance of High Strength 6082 Alloys Consider Extrudability and Small Modifications of the Profile Geometry. *Mater. Today Proc.* **2019**, *10*, 193–200. [[CrossRef](#)]
3. Hu, J.; Zhang, W.; Fu, D.; Teng, J.; Zhang, H. Improvement of the mechanical properties of Al–Mg–Si alloys with nano-scale precipitates after repetitive continuous extrusion forming and T8 tempering. *J. Mater. Res. Technol.* **2019**, *8*, 5950–5960. [[CrossRef](#)]
4. Wang, X.F.; Shi, T.Y.; Wang, H.B.; Zhou, S.Z.; Xie, C.; Wang, Y.G. Mechanical behavior and microstructure evolution of Al-Mg-Si-Cu alloy under tensile loading at different strain rates. *Mater. Res. Express* **2019**, *6*, 15. [[CrossRef](#)]
5. Sekhar, A.P.; Mandal, A.B.; Das, D. Mechanical properties and corrosion behavior of artificially aged Al-Mg-Si alloy. *J. Mater. Res. Technol.-JMRT* **2020**, *9*, 1005–1024. [[CrossRef](#)]
6. Farh, H.; Djemmal, K.; Guemini, R.; Serradj, F. Nucleation of dispersoids study in some Al-Mg-Si alloys. *Ann. Chim.-Sci. Mater.* **2010**, *35*, 283–289. [[CrossRef](#)]
7. Mao, H.; Kong, Y.; Cai, D.; Yang, M.; Peng, Y.; Zeng, Y.; Zhang, G.; Shuai, X.; Huang, Q.; Li, K.; et al. β'' needle-shape precipitate formation in Al-Mg-Si alloy: Phase field simulation and experimental verification. *Comput. Mater. Sci.* **2020**, *184*, 109878. [[CrossRef](#)]
8. Yang, M.; Chen, H.; Orekhov, A.; Lu, Q.; Lan, X.; Li, K.; Zhang, S.; Song, M.; Kong, Y.; Schryvers, D.; et al. Quantified contribution of β'' and β' precipitates to the strengthening of an aged Al–Mg–Si alloy. *Mater. Sci. Eng. A* **2020**, *774*, 138776. [[CrossRef](#)]
9. Chakrabarti, D.J.; Laughlin, D.E. Phase relations and precipitation in Al–Mg–Si alloys with Cu additions. *Prog. Mater. Sci.* **2004**, *49*, 389–410. [[CrossRef](#)]
10. Sunde, J.K.; Marioara, C.D.; van Helvoort, A.T.J.; Holmestad, R. The evolution of precipitate crystal structures in an Al-Mg-Si(-Cu) alloy studied by a combined HAADF-STEM and SPED approach. *Mater. Charact.* **2018**, *142*, 458–469. [[CrossRef](#)]
11. Sunde, J.K.; Marioara, C.D.; Holmestad, R. The effect of low Cu additions on precipitate crystal structures in overaged Al-Mg-Si(-Cu) alloys. *Mater. Charact.* **2020**, *160*, 110087. [[CrossRef](#)]
12. Wang, Y.; Fang, C.M.; Zhou, L.; Hashimoto, T.; Zhou, X.; Ramasse, Q.M.; Fan, Z. Mechanism for Zr poisoning of Al-Ti-B based grain refiners. *Acta Mater.* **2019**, *164*, 428–439. [[CrossRef](#)]
13. Babaniaris, S.; Ramajayam, M.; Jiang, L.; Varma, R.; Langan, T.; Dorin, T. Effect of Al₃(Sc,Zr) dispersoids on the hot deformation behaviour of 6xxx-series alloys: A physically based constitutive model. *Mater. Sci. Eng. A* **2020**, *793*, 139873. [[CrossRef](#)]
14. Meng, Y.; Cui, J.; Zhao, Z.; He, L. Effect of Zr on microstructures and mechanical properties of an AlMgSiCuCr alloy prepared by low frequency electromagnetic casting. *Mater. Charact.* **2014**, *92*, 138–148. [[CrossRef](#)]
15. Vlach, M.; Cizek, J.; Smola, B.; Melikhova, O.; Vlcek, M.; Kodetova, V.; Kudrnova, H.; Hruska, P. Heat treatment and age hardening of Al-Si-Mg-Mn commercial alloy with addition of Sc and Zr. *Mater. Charact.* **2017**, *129*, 1–8. [[CrossRef](#)]
16. Fu, J.N.; Yang, Z.; Deng, Y.L.; Wu, Y.F.; Lu, J.Q. Influence of Zr addition on precipitation evolution and performance of Al-Mg-Si alloy conductor. *Mater. Charact.* **2020**, *159*, 7. [[CrossRef](#)]
17. Himuro, Y.; Koyama, K.; Bekki, Y. Precipitation Behaviour of Zirconium Compounds in Zr-Bearing Al-Mg-Si Alloy. *Mater. Sci. Forum* **2006**, *519–521*, 501–506. [[CrossRef](#)]
18. Li, L.; Zhang, Y.; Esling, C.; Jiang, H.; Zhao, Z.; Zuo, Y.; Cui, J. Crystallographic features of the primary Al₃Zr phase in as-cast Al-1.36wt% Zr alloy. *J. Cryst. Growth* **2011**, *316*, 172–176. [[CrossRef](#)]
19. Cvahte, P.; Jelen, M.; Dragojevič, V.; Steinacher, M. A High-Strength Al-Mg-Si Aluminium Alloy and Its Manufacturing Process. European Patent Office EP3214191A1, 19 August 2020.
20. Zupanič, F.; Steinacher, M.; Bončina, T. As-cast microstructure of a novel Al-Mg-Si alloy. *Livar. Vestn.* **2019**, *66*, 125–136.
21. Du, Y.; Chang, Y.A.; Huang, B.Y.; Gong, W.P.; Jin, Z.P.; Xu, H.H.; Yuan, Z.H.; Liu, Y.; He, Y.H.; Xie, F.Y. Diffusion coefficients of some solutes in fcc and liquid Al: Critical evaluation and correlation. *Mater. Sci. Eng. A-Struct. Mater. Prop. Microstruct. Process.* **2003**, *363*, 140–151. [[CrossRef](#)]
22. Zupanič, F.; Gspan, C.; Burja, J.; Bončina, T. Quasicrystalline and L12 precipitates in a microalloyed Al-Mn-Cu alloy. *Mater. Today Commun.* **2020**, *22*, 100809. [[CrossRef](#)]
23. Han, Y.; Ma, K.; Li, L.; Chen, W.; Nagaumi, H. Study on microstructure and mechanical properties of Al–Mg–Si–Cu alloy with high manganese content. *Mater. Des.* **2012**, *39*, 418–424. [[CrossRef](#)]